

Functional Connectivity of Organic Neuromorphic Devices by Global Voltage Oscillations

Dimitrios A. Koutsouras, Themis Prodromakis, George G. Malliaras, Paul W. M. Blom, and Paschalis Gkoupidenis*

Global oscillations in the brain synchronize neural populations and lead to dynamic binding between different regions. This functional connectivity reconfigures as needed for the architecture of the neural network, thereby transcending the limitations of its hardwired structure. Despite the fact that it underlies the versatility of biological computational systems, this concept is not captured in current neuromorphic device architectures. Herein, functional connectivity in an array of organic neuromorphic devices connected through an electrolyte is demonstrated. The output of these devices is shown to be synchronized by a global oscillatory input despite the fact that individual inputs are stochastic and independent. This temporal coupling is induced at a specific phase of the global oscillation in a way that is reminiscent of phase locking of neurons to brain oscillations. This demonstration provides a pathway toward new neuromorphic architectural paradigms, where dynamic binding transcends the limitations of structural connectivity, and could enable architectural concepts of hierarchical information flow.

1. Introduction

Neurons in the brain are connected with each other with an immense number of synapses, and this structural connectivity plays a central role in the brain's computational power.

Dr. D. A. Koutsouras, Prof. P. W. M. Blom, Dr. P. Gkoupidenis
Molecular Electronics Workgroup
Max Planck Institute for Polymer Research
Ackermannweg 10, 55128 Mainz, Germany
E-mail: Gkoupidenis@mpip-mainz.mpg.de

Prof. T. Prodromakis
Electronic Materials and Devices Research Group
Zepler Institute
University of Southampton
University Road, Southampton SO17 1BJ, UK

Prof. G. G. Malliaras
Electrical Engineering Division
Department of Engineering
University of Cambridge
9 JJ Thomson Ave, Cambridge CB3 0FA, UK

 The ORCID identification number(s) for the author(s) of this article can be found under <https://doi.org/10.1002/aisy.201900013>.

© 2019 The Authors. Published by WILEY-VCH Verlag GmbH & Co. KGaA, Weinheim. This is an open access article under the terms of the Creative Commons Attribution License, which permits use, distribution and reproduction in any medium, provided the original work is properly cited.

DOI: 10.1002/aisy.201900013

Neuroplasticity in the brain spans in a range of timescales and has a plethora of implications, from neuronal development to signal processing.^[1] In addition to this anatomical connectivity, higher order phenomena exist that determine the way information is conveyed and processed in the brain. These phenomena contribute to the dynamic linking of different neural ensembles or even distant areas in the brain. This dynamic linking is mainly mediated by extracellular/macroscopic voltage oscillations.^[2,3] Oscillations arise from the collective activity of large neural populations (bottom-up approach), and among various functions, these oscillations synchronize the activity of neural ensembles (top-bottom approach) (Figure 1a shows a simplified schematic of synchronization).^[4-6]

In biological neural networks, synchronization and transient modulation of neuronal

gain through global oscillations, permits the top down control of the activity of a neural population or between populations.^[6] Synchronization of distant regions in the brain constitutes a form of functional connectivity between neural ensembles that transcends the structural connectivity of the network.^[7] At the processing level, global oscillation-mediated synchronization preserves the temporal relationship between parallel inputs of stochastic activities, thus enhancing the salience of neural networks. Therefore, the ability of the sensory system to process inputs selectively in specific time windows is pronounced in cases such as attention during learning.^[6-10] The cross-coupling of various oscillations in the brain is also of significant importance, with fast oscillations to be nested on slower ones. This coupling constitutes a powerful mode of signal multiplexing that allows multiregional binding in the brain for integrating spatially distributed or even heterogeneous signals.^[2,8,11,12] At an even higher level, synchronization phenomena and neural oscillations are related to cognitive functions such as working memory, perception, and coordination of motor tasks.^[4,10,13]

This inherent capability of the brain to cope with the processing of heterogeneous, loosely structured, or even unstructured signals constitutes the most efficient computational paradigm for biomimicry. Emulating the working of the brain at the hardware-based level is not only necessary for overcoming the limitations of conventional complementary metal-oxide semiconductor (CMOS) technology based on the traditional von Neumann architecture, but also essential to understand

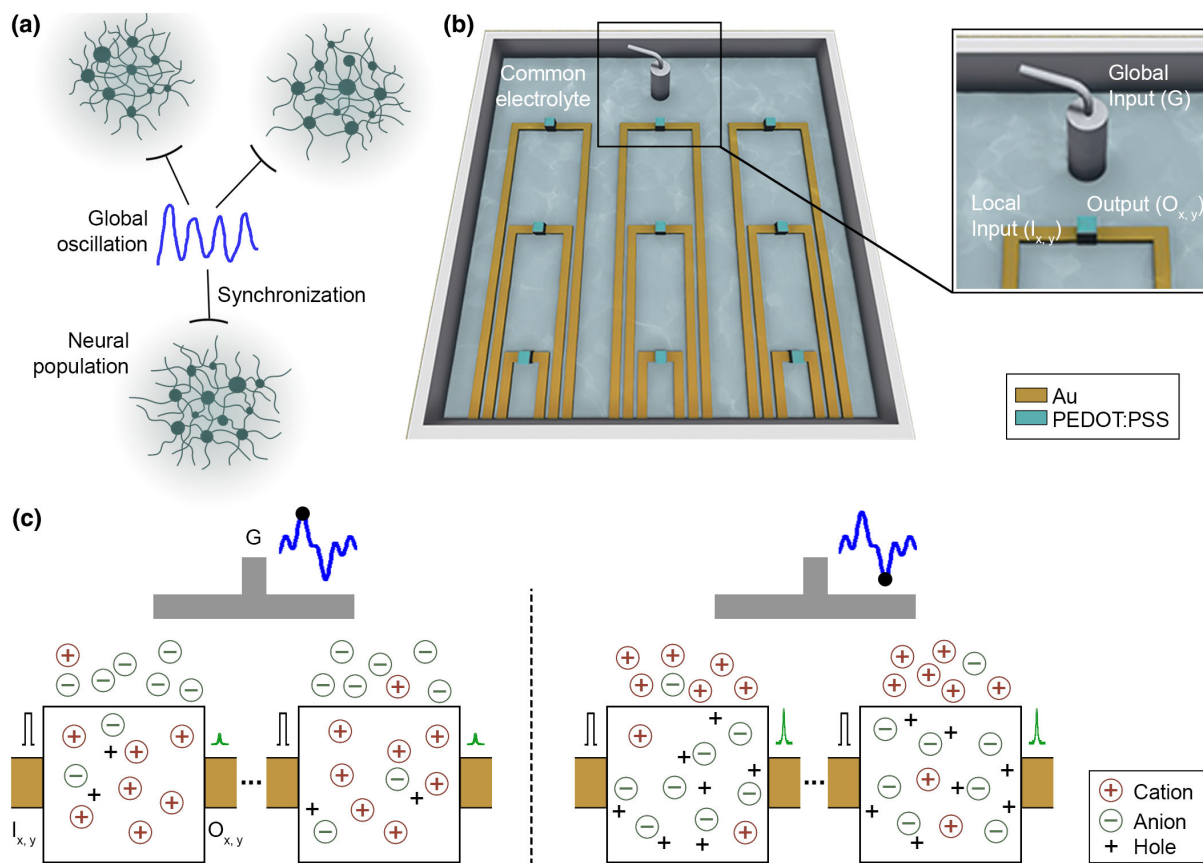


Figure 1. Synchronization of neural populations and the corresponding device behavior. a) Schematic of synchronization of neural populations in biological neural networks through global voltage oscillations. The activity of distant neural populations can be temporally coupled with a global voltage oscillation. Synchronization occurs due to the collective modulation of the membrane potential of the population. b) Schematic of the device grid. The grid consists of 3×3 , two-terminal PEDOT:PSS-based devices in a square-like configuration (with $x = 1-3$ and $y = 1-3$, device coordinates). The external metal lines are covered with a dielectric, but not shown here for simplicity. The grid is immersed in a common electrolyte and a global input G is used to collectively address the devices. At the single device level, one terminal of the device is the local input $I_{x,y}$ and the other is the local output $O_{x,y}$. c) Schematic of the synchronization process of an array of PEDOT:PSS devices that share a common electrolyte through a global voltage oscillation G . Left panel: At a phase of the global oscillation that corresponds to the amplitude maximum of G , cations are injected from the electrolyte into the channel and the hole density is decreased (and the resulting output current $O_{x,y}$ of a local input $I_{x,y}$ is calculated). Right panel: At a phase of the global oscillation that corresponds to the minimum of G , cations are extracted from the channel and hole density is increased (and the corresponding $O_{x,y}$ is calculated). For a random sequence of input signals $I_{x,y}$, synchronization is favorable for the amplitude minimum of G .

its function by adopting a reverse engineering approach. Neuromorphic computing or engineering, a term that was first introduced in the 1990s by C. Mead, constitutes the basis for hardware-based neuroinspired information processing.^[14] Among other technologies, organic materials have recently emerged for neuromorphic engineering and are regarded as strong candidates, especially for interacting with the human sensory system and for adaptable biointerfacing.^[15–19] A key aspect of organic materials is their ability to conduct both ionic and electronic carriers (i.e., organic mixed conductors),^[20] which enables organic devices to operate in electrolytes, a feature that resembles the biological environment. By leveraging the properties of organic mixed conductors at the device level, a variety of neuromorphic functions for neuroinspired information processing has been recently demonstrated, including short- and long-term potentiation/depression,^[21–26] low-energy analog switching,^[23,25–28] device integration with biological substances,^[29,30] neuromorphic sensing,^[31–33] perceptron-based artificial

neural networks,^[34–36] and spatially correlated functions.^[37,38] Although the field of neuromorphic engineering has rapidly advanced over the past years, the mainstream strategy in neuromorphic devices is mostly concentrated on the emulation of neuroplasticity forms, learning rules such as Hebbian learning and spike-timing-dependent plasticity (STDP), and neuron-like models with a variety of device technologies, either organic or inorganic.^[17,39–42] Regarding the abovementioned neuromorphic devices, it is worth mentioning that most architectures rely on hardwired devices; unlike in the brain, there also exist mechanisms on top of structural connectivity, such as global oscillation-mediated synchrony, which promote functional connectivity. Recently, the concept of “soft” connectivity through continuous media for neuromorphic architectures has been demonstrated.^[43,44] In the proposed “soft” connectivity concept, neuromorphic behavior was mainly focused on connectivity functions based on the static coupling between devices and/or device terminals. However, functional connectivity in biological

neural processing allows the precise temporal binding of spatially distributed subunits. At the architectural level, this allows for functional connectivity between subunits in a dynamic and hardware-independent approach. Contrary to the mainstream approach of neuroplasticity or structural connectivity, the emulation of functional or dynamic connectivity is largely unexplored in neuromorphic device architectures, although it has major implications in biological neural processing.

A functional type of connectivity between organic neuromorphic devices is demonstrated in this work. An array of neuromorphic devices is used, with each receiving independent, random input signals. The devices are immersed in a common electrolyte through which a global oscillatory input is applied. This oscillatory input emulates global voltage oscillations in biological networks, and it is forced externally (top-bottom approach). It is shown that device output is synchronized with the global rhythm, with “clustering” at its amplitude extrema. This synchronization becomes more pronounced in devices receiving input more frequently. Although the devices are not hardware-connected with each other, they exhibit global temporal coupling that is entrained by the global oscillation. These results resemble phase locking of neurons to brain oscillations. The functional connectivity achieved through the common electrolyte can lead to new architectural paradigms of dynamic or transient linking of spatially distributed parts in a circuit without the need for structural connectivity between them.

2. Results

2.1. Global Oscillations as Synchronization Functions

The device configuration is depicted in Figure 1b. It consists of a square grid of 3×3 , two-terminal poly(3,4-ethylenedioxythiophene) doped with poly(styrene sulfonate) (PEDOT:PSS) devices. The fabrication process is described in the experimental section. Briefly, each device is made of a photolithographically defined PEDOT:PSS channel and external Au lines. Each PEDOT:PSS channel has nominal dimensions of $50 \times 50 \mu\text{m}$ (width \times length, $W \times L$), and every device is placed at a center-to-center device distance of $5000 \mu\text{m}$. The film thickness of PEDOT:PSS is $\approx 250 \text{ nm}$. External Au lines are insulated, and only the active area of each device (PEDOT:PSS film) is not protected from the insulator (for simplicity, insulation is not shown in Figure 1b). The grid is exposed to a common NaCl electrolyte (100 mM) and global Ag/AgCl electrode is immersed into the electrolyte. At the single device level, one terminal of the device is the local input ($I_{x,y}$) and the other is the output ($O_{x,y}$), where x and y are the indexes of the 3×3 grid. The Ag/AgCl electrode acts as the global input (G) of the grid. During electrical measurements, an input voltage signal is applied at each local input $I_{x,y}$ and the resulting output current is measured at each output $O_{x,y}$ terminal, while being grounded, with a semiconductor analyzer. A global voltage oscillation is also applied at the gate electrode G . The global voltage oscillation leads to rhythmic injection/extraction of mobile ions of the NaCl electrolyte, from/to the electrolyte to/from the PEDOT:PSS-based devices and thus leading to a rhythmic doping/dedoping of the PEDOT:PSS channels.^[44–46] This global oscillation leads to a periodic modulation of the resistance of the PEDOT:PSS channels that depends on the temporal

form of the oscillation G (see also Figure 1c and Figure S1, Supporting Information for the temporal evolution of the device conductance under the influence of the global oscillation G and Figure S2, Supporting Information, for the device stability during an experiment).^[44] Due to the common nature of the electrolyte and the Ag/AgCl electrode, the resistance of the PEDOT:PSS channels of the 3×3 grid is modulated in a parallel manner, and all devices are addressed in a collective way.^[47] With this configuration, when an arbitrary voltage pattern is applied at each local input $I_{x,y}$, the corresponding output $O_{x,y}$ of the devices preserves the temporal content of the global oscillation G , and therefore, synchronization of the device grid is possible (an example of two devices is shown in Figure 1c).

2.2. Global/Local Temporal Coupling

Figure 2a shows how a random sequence voltage signals at the local input I_i (index i refers to a single device on the 3×3 grid) can be synchronized with a global voltage oscillation G . At the single device level, the following measurement protocol is used: a random sequence of square voltage pulses is applied at the local input I_i (with amplitude $V_i = 50 \text{ mV}$, width $t_p = 50 \text{ ms}$, and for different pulse numbers $N = 2–350$), and the resulting output current is measured at the O_i terminal (a schematic of the derivation process of the random sequence of voltage pulses is shown in Figure S3, Supporting Information). A voltage oscillation is also applied at the global terminal G where the amplitude modulation (AM) of a carrier signal with a modulation signal (AM of a carrier sine wave of frequency of $f_c = 1 \text{ Hz}$ was achieved, with a modulation sine wave of frequency $f_M = 3 \text{ Hz}$, refer also to Supplementary Information). Figure 2a shows the output response of a device O_i when a random sequence of pulses with $N = 10, 100$, and 350 is applied at the local input I_i , under the influence of the global oscillation G (detailed O_i response as a function of $N = 2–350$ is presented in Figure S4, Supporting Information). Even though the input signal I_i is random in terms of instantaneous frequency, a tight temporal coupling between the global oscillation G and the resulting output O_i is observed. This coupling is pronounced at the amplitude minimum of the global signal G (whenever there is a significant overlap between the random input I_i and the amplitude minimum of G). The results of phase-normalized, spike analysis of the output O_i as a function of the number N of local input pulses I_i ($N = 10, 100$, and 350) is presented in Figure 2b. The peak distribution as a function of the phase of the global signal G is shown in Figure 2b. The results of detailed peak analysis and the phase normalized, spike distribution of O_i as a function of N are presented in Figures S5 and S6, Supporting Information, respectively. Indeed, from Figure 2b, it is evident that as the number N of random input pulses increases, distribution of O_i spike is generated with a mean value that is centered at specific phase of G that corresponds to the amplitude minimum of G . Phase-dependent synchronization of neuronal ensembles through global oscillations or even phase locking, similar to that shown in Figure 2b, is also observed in biological neural networks.^[4,48,49] It is noteworthy that in the present case, synchrony occurs at a phase of the global signal of $\approx 1.25 \pi$, which corresponds to the minimum amplitude G (see also Figure 1).

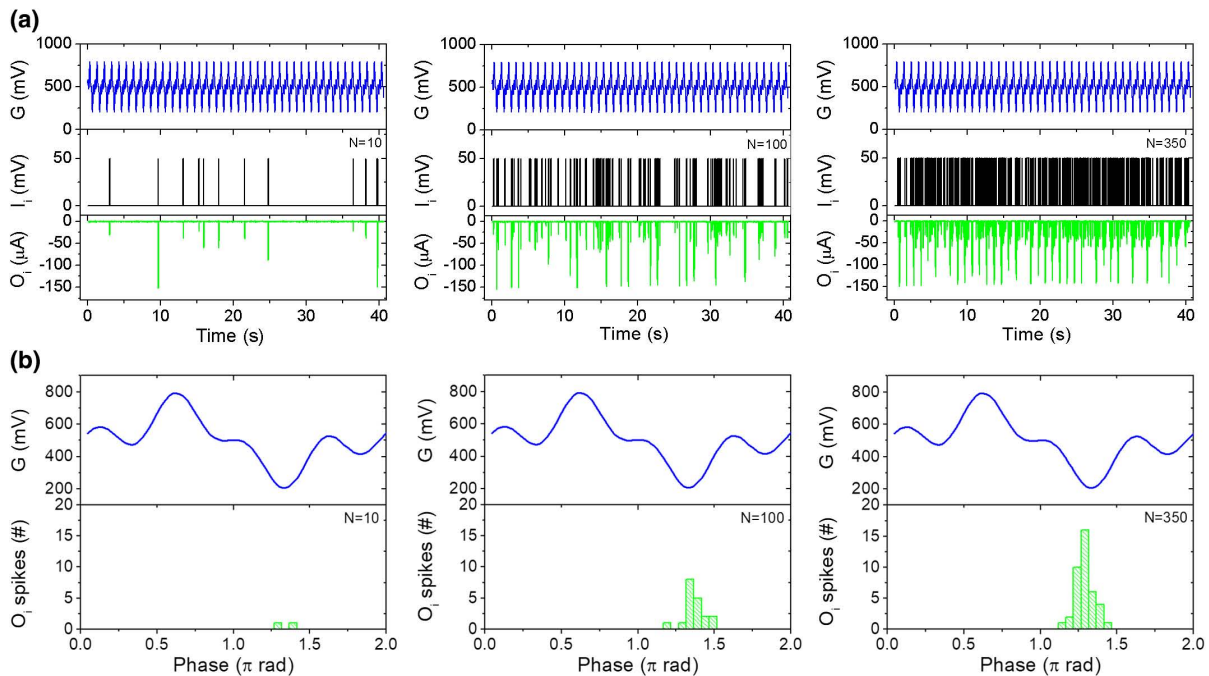


Figure 2. Temporal coupling of a random input with a global voltage oscillation at the single device level. a) A random sequence of square pulses at the local input I_i (amplitude $V_i = 50$ mV, width $t_p = 50$ ms, and for different pulse numbers $N = 10, 100$, and 350) is synchronized with a global voltage oscillation G (AM of a carrier sine wave of frequency $f_C = 1$ Hz, with a modulation sine wave of frequency $f_M = 3$ Hz). The temporal coupling between I_i and G appears as a time-correlated spike of O_i that coincides with the minimum of the global voltage oscillation. b) Phase-normalized, spike distribution of O_i is defined in Figure 2a for different pulse numbers N . The temporal relationship between an irregular input I_i and the global oscillation G is preserved, as shown from the spike distribution of O_i that has a mean value at a specific phase of G , that is, the minimum of voltage amplitude.

Although there is a qualitative similarity in the device behavior and in synchrony of biological neural networks, in the latter case synchrony may also occur in different phases of the global oscillation.

2.3. Single Device Synchrony through Global Oscillations

Figure 3a shows clearly that the temporal window of communication between local input I_i and O_i is preserved through the global oscillation G (for random pulses at the local input with $N = 250$, amplitude $V_i = 50$ mV, and width $t_p = 50$). Time vs frequency analysis of O_i (short-time Fourier transform [STFT], a common method for studying spectral distribution of neural activity in the field of neuroscience),^[3] indicates high power/frequency activity at a window that corresponds to the amplitude minimum of G , even though the local input consists of random pulses (time vs frequency analysis of O_i as a function of the number N of input pulses, which is shown in Figure S7, Supporting Information). These high activity areas express discrete epochs during which communication between I_i and O_i is maximum, or more precisely, a time-locking behavior of output O_i through the global oscillation G . The communication window is also evident in Figure 3b, which shows the number of O_i spikes as a function of the number N ($=2-350$) of the random I_i pulses for 40 global signal cycles (O_i spikes were detected from peak analysis as shown in Figure S5, Supporting Information). For more repetitive random sequences of pulses at the local input

(or as N is increased), there is a synchronization event in almost every cycle of the global oscillation G , and thus, the number of output O_i spikes approaches the total number of G cycles (inset of Figure 3b shows a synchronization event at the local minimum of G for an intermediate number of random pulses N), as also shown in the right y-axis of Figure 3b (expresses the percentage of synchronization events with respect to the total number of global cycles). The non-strict monotonic behavior shown in Figure 3b is attributed to the randomness of the input signal. The analysis of Figure 3b is expanded for the device array, and the corresponding statistics are shown in Figure S8, Supporting Information.

Due to the fact that time locking or synchronization is enhanced for more repetitive random inputs, this is also reflected in the correlation between the global oscillation G and the output O_i .^[7] Statistical correlation coefficient of the global input and output as a function of the number N of random input pulses is shown in Figure 3c. Because the appearance of a synchronization event is more probable for dense input signals at I_i (see also Figure 3b), correlation coefficient also increases with an increase in N . Similar to Figure 3b, deviation from strict monotonic behavior is attributed to the randomness of the input signal. Figure 3d shows the calculated correlation function of global input G and output O_i as a function of the number N ($=2-350$). This time-dependent correlation of G and O_i reveals how a single device becomes entrained to a specific rhythm that is defined by the global oscillation. Similar to the correlation

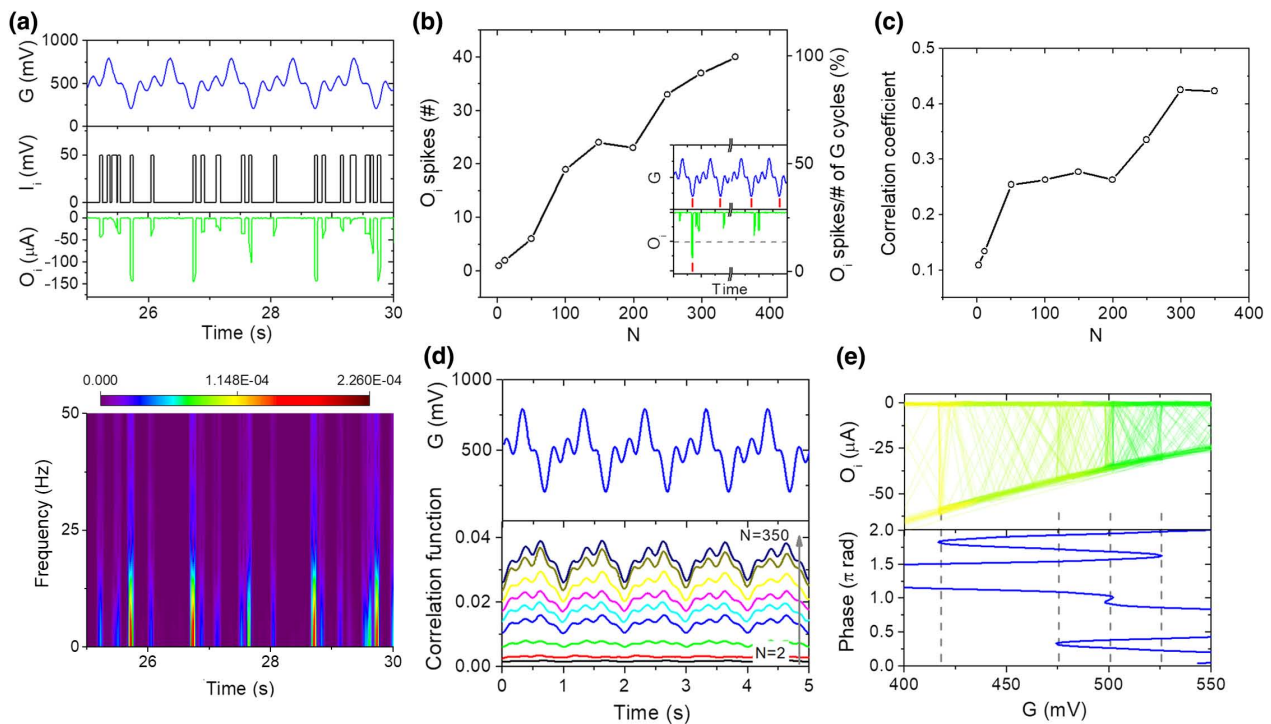


Figure 3. Single device synchrony. a) Upper panel: Detailed synchronization response of a sequence of squared random pulses at the local input I_i (amplitude $V_i = 50$ mV, width $t_p = 50$ ms, and for $N = 250$) with the global voltage oscillation G (AM of a carrier sine wave of frequency $f_C = 1$ Hz with a modulation sine wave of frequency $f_M = 3$ Hz). Lower panel: Time vs frequency analysis of O_o , as results from STFT of O_o (color map corresponds to the power of the output signal). High power/frequency areas correspond to the amplitude minimum of the global oscillation G . b) O_o spikes as a function of the number N of the input random pulses for 40 cycles of the global signal (the right y-axis expresses the percentage of synchronization events with respect to the total number of global cycles). The inset graph shows an example of a synchronization event between G and O_o signals and a few escapes from synchronization. The number of synchronization events approaches the number of G cycles for a large number of N . c) Correlation coefficient between G and O_o as a function of N . Similar to Figure 3b, correlation coefficient increases with N . d) Correlation function between G and O_o for different numbers of random pulses N (2–350) for the first 5 cycles of G . Correlation function is increased with N . As N is increased, a maximum correlation between G and O_o appears at the window of the amplitude minimum of G , where synchronization occurs. e) O_o vs G graph (Lissajous diagram) with respect to the phase vs G curve of the global oscillation for $N = 350$. Weak O_o spike clustering is observed at the local extrema of the global signal G .

coefficient calculated from Figure 3c, correlation function shown in Figure 3d is increased for denser local input signals I_i . Even more interestingly for large N values (e.g., $N = 350$), time dependence of the correlation function displays a maximum close to the synchronization regime of the global oscillation (i.e., the minimum of the signal). This behavior further supports the tight temporal coupling of a single device output O_o with the global signal G at a specific phase of the latter (the correlation function for the device grid is shown in Figure S12, Supporting Information).

The correlation of the global signal G with a single device output O_o is also observed at the local minima/maxima of the global signal G . For instance, in Figure 3e, the O_o vs G or Lissajous diagram is shown with respect to the phase vs G curve of the global oscillation for $N = 350$ (similar diagrams as a function of the number of input pulses N are shown in Figure S9, Supporting Information). Weak O_o spike clustering is evident at the local extrema of the global signal G (also shown as vertical dashed lines in the lower panel of Figure 3e). Despite the stochastic nature of local input I_i in terms of instantaneous frequency, O_o spikes of specific amplitude are accumulated or clustered at the

local extrema of G . In other words, these local extrema can be regarded as amplitude selectors of a stochastic sequence of input pulses at I_i , with different local extrema that tend to create segregation in the amplitude of O_o spikes. This behavior is attributed to an increased probability of spike accumulation (overlap between I_i and G) at the local extrema than in areas with monotonic change of G . This weak spike clustering is observed in every device of the array, although each device receives a unique sequence of random pulses (additional Lissajous diagrams for the device array and for the number of pulses $N = 350$ are shown in Figure S10, Supporting Information).

2.4. Phase-Dependent Synchrony Promotes Functional Connectivity between Devices

Synchrony of a device population (a grid of 3×3 devices, with coordinates $x = 1-3$ and $y = 1-3$) is shown in Figure 4. The same measurement protocol as shown in Figure 2 is followed in Figure 4 for every device of the grid. Briefly, a sequence of N random pulses is applied at the local input of every device

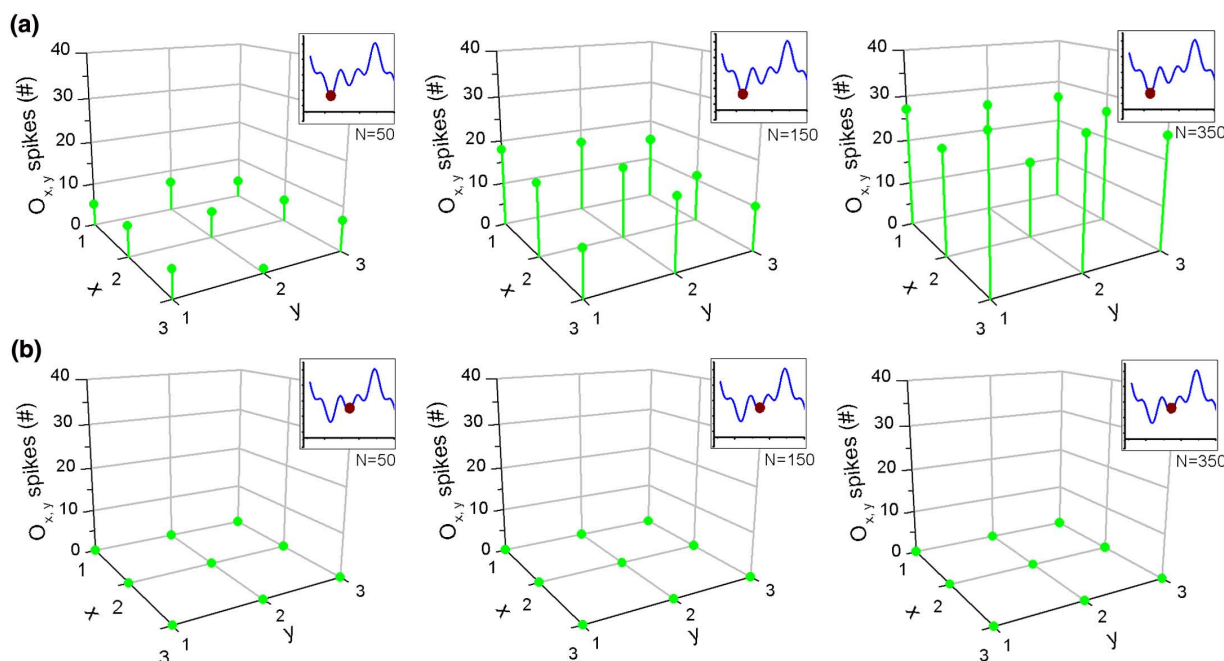


Figure 4. Output synchrony of a device population. a) Total number of $O_{x,y}$ spikes of the 3×3 device grid ($x = 1-3$ and $y = 1-3$) at the phase of the global oscillation in which synchronization is observed for a sequence of random pulses with numbers $N = 50, 150$, and 350 (for a given number N , inputs $I_{x,y}$ are stochastic and non-correlated from device to device). b) Total number of $O_{x,y}$ spikes of the device grid at the phase of the global oscillation that is outside the synchronization window for $N = 50, 150$, and 350 . A tight global and temporal alignment is observed between G and $O_{x,y}$ at the synchronization window of the global oscillation G .

$I_{x,y}$, the global voltage oscillation is applied at the G terminal, and the output $O_{x,y}$ of every device is measured as a function of time. It should be noted that for the same number of pulses N , a completely random and non-correlated pulse sequence is applied to different devices on the grid. From the peak analysis of every device, a phase-normalized, spike analysis of the output $O_{x,y}$ as a function of the number N is performed (see also Figure S11, Supporting Information). Figure 4a shows the total number of $O_{x,y}$ spikes of the device grid at the phase of the global oscillation in which synchronization is observed for $N = 50, 150$, and 350 . The same result is shown in Figure 4b for a phase of the global oscillation G that is distant from synchronization window. The global oscillation structures the coupling of the output $O_{x,y}$ of the device grid with G , and the device population is entrained to the rhythm of G despite the stochastic nature (noncorrelation) of the random pulses $I_{x,y}$ from device to device. For out-of-synchronization phase, the coupling between G and $O_{x,y}$ is suppressed as shown in Figure 4b. It should be noted that a device response is independent of the position of the global Ag/AgCl electrode, as confirmed by impedance spectroscopy measurements of a single device by placing the gate electrode at different positions on the device grid (Figure S12, Supporting Information).^[44,47] This behavior is attributed to the faradaic response of the global gate electrode. When a voltage is applied at an electrode with a faradaic response (i.e., an ohmic contact between the gate and the electrolyte), the potential drop at the electrolyte is negligible,^[50] and the overall device behavior is practically independent of the distance between the gate electrode and the device.

The concept of synchrony of the device population is further supported by mapping the global coherence of the device grid. For this purpose, the correlation function ξ (between the global input G and each output $O_{x,y}$) of the device grid is mapped, as shown in Figure 5, for two different phases of the global oscillation G and for various numbers of random pulses at the local inputs $I_{x,y}$ ($N = 50, 150$, and 350) of each device of the grid. Figure 5a shows the correlation function of mapping at the synchronization phase of G , while mapping outside the synchronization window is shown in Figure 5b (detailed correlation function as a function of time for various number N of random pulses for the device grid is shown in Figure S13, Supporting Information). In both phase cases shown in Figure 5a,b, the correlation function increases with an increase in N . Nevertheless, devices show higher correlation for the phase mapping corresponding to synchronization than for the phase mapping outside synchronization window (e.g., the upper right graph in comparison to the lower right one of Figure 5). It is worth noting that correlation mappings are fairly homogeneous, meaning that for a specific phase, the correlation between G and $O_{x,y}$ is similar; and consequently, the correlation between different devices that receive independent (non-correlated) inputs $I_{x,y}$ is tightly preserved.

3. Discussion

This work demonstrated how functional connectivity of a grid of two terminal PEDOT:PSS-based devices can be induced with a global voltage oscillation. In biological neural networks,

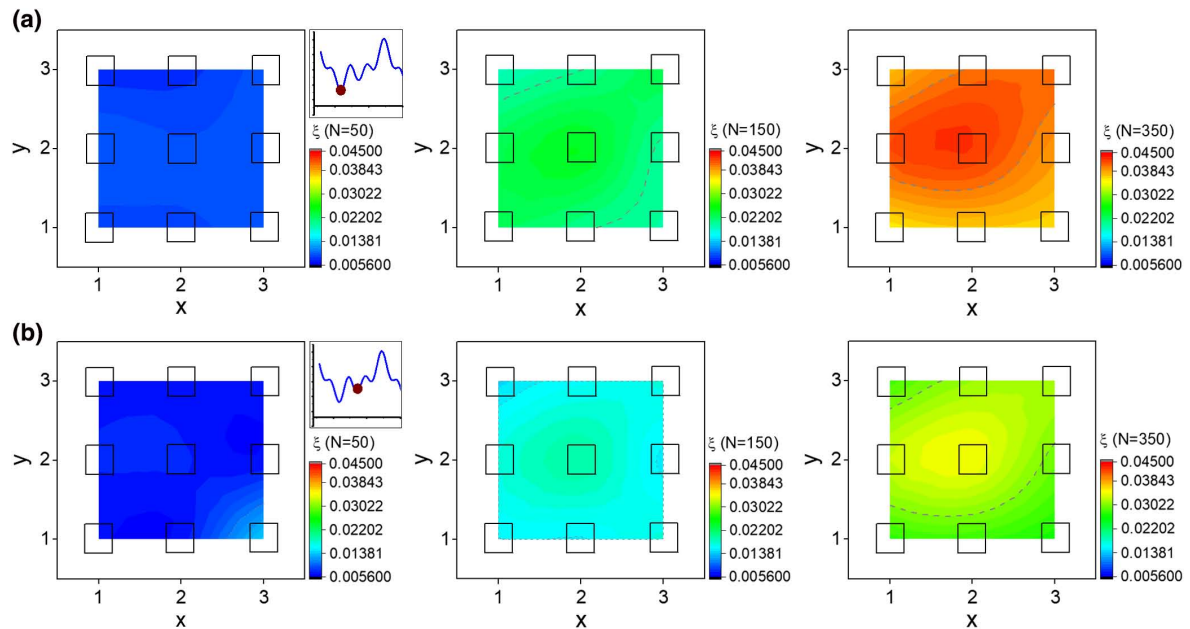


Figure 5. Global coherence of a device population. Spatial mapping of correlation function ξ (between the global input G and each output $O_{x,y}$) of the 3×3 device grid ($x = 1-3$ and $y = 1-3$) for two different phases of the global oscillation G and for various number of random pulses at the local inputs $I_{x,y}$ ($N = 50, 150$, and 350) of each device on the grid (for a given number N , inputs $I_{x,y}$ are stochastic and noncorrelated from device to device). Spatial mapping of correlation function ξ : a) at the synchronization phase and b) outside the synchronization phase of G . Correlation function map is drawn for in-phase response and for large numbers N . In any case, spatial mapping is fairly homogenous, meaning that correlation between G and each $O_{x,y}$ and therefore from device to device, is global.

functional connectivity has tremendous impact on neural processing as it defines how signals between different brain regions are associated with integrating heterogeneous information (e.g., vision and motor control). To summarize, functional connectivity is of great importance in biological neural networks because it allows for spatiotemporal addressing and association of distributed regions in the brain through global oscillations and traveling waves. These phenomena are complementary to structural connectivity and allow for time-resolved, distributed processing in the brain. This behavior is in analogy with macroscopic voltage oscillations in biological neural networks that are produced from the collective synchrony of neural ensembles.^[3,48] At the single device level, the global oscillation provides a temporal window of synchronization at a specific phase of G , as shown from time vs frequency analysis of the output signal O_i and the correlation function between the global signal G and the output O_i . For higher-order harmonics, global signal G such as the one that is used in the study, weak O_i spike nesting is observed at phases that correspond to the local extrema of G . Because the electrolyte is common for the device grid, a tight temporal coupling between the global signal G and each output $O_{x,y}$ of the grid is observed and consequently between the devices. This global addressing is manifested as a G phase-correlated, collective activity of $O_{x,y}$ and a homogenous modulation of the correlation function between G and each output $O_{x,y}$ at the device grid level.

The concept of synchronization or similar neuroinspired functions may add in the future more biologically plausible features in neuromorphic device architectures beyond the well-established neuroplasticity forms. At the device or architecture

level, similar global oscillations G could be used in an array of electrochemical memory devices^[21-23,25,51] in order to collectively modulate the threshold of memory and thereby change the long-term memory state only in specific phases of G by using additional local inputs $I_{x,y}$. In this way, phase-dependent learning/training features can be introduced in analogy with attention during biological learning processes. In addition, bottom-up synchrony in analogy with synchronized neural populations can be achieved, as elementary oscillators based on simple electrochemical devices already exist.^[52] Moreover, traveling waves of ionic species in electrolytes could be leveraged^[53-55] for introducing entirely novel neuromorphic concepts in device addressing, in analogy with traveling waves in the brain.^[56,57] These concepts include spatiotemporal device addressing such as propagation of synchrony in space and spatial addressing through wave interference phenomena in a common electrolyte that is shared to a device array. Moreover, electrolyte-gating is “universal,” and therefore, it can be used to gate various devices made of single crystal, ferroelectric, polymer, and 1D or 2D materials. Finally, the concept of synchrony can be adopted for introducing neuromorphic synchronization features in bioelectronics. For instance, the proposed structure could be placed between a recording and a stimulation platform of biological cell cultures in order to propagate synchrony from the former to the latter one.

4. Experimental Section

Device Fabrication: First, the substrates, 25 m \times 76 mm optical microscope glass slides, were assiduously cleaned in a soap sonication bath for 15 min

followed by 15 min of sonication in an organic solvent mixture (acetone/isopropanol 1:1 vol/vol). Subsequently, device electrodes and pads were patterned with standard photolithography techniques. A positive photoresist (S 1813) was spun on the substrate, and the created film was first exposed to UV light through a photolithography mask and then developed using MF-26 developer. Gold was then deposited on the substrate with the help of a sputtering coating system. The subsequent lift-off step in acetone/isopropanol resulted in 100 nm gold features patterned on the substrate, while a 10 nm chromium layer used as an adhesion promoter between gold and substrate. Afterward, the devices were encapsulated in a double, 2 μm each, parylene C layer that plays the role of both electrical insulator and electrolyte shield. Between these layers, a 2% soap (Micro-90) solution would serve as an anti-adhesive promoter in a later fabrication stage. A second photolithography step was employed to define the 50 μm \times 50 μm channel (width \times length, $W \times L$) on each device (the devices form a regular 3 \times 3 grid with a spacing of 5000 μm between adjacent devices). A different positive photoresist (AZ 9260) was spun on top of the two parylene C layers, and after UV exposure and development steps, windows were defined in the photoresist film. Through these windows, parylene C was etched away via O_2 plasma reactive ion etching, resulting in the creation of wells across the parylene C layer. The PEDOT:PSS film was then deposited on the patterned substrate through spin-coating (at 3500 rpm for 30 s) from dispersion solution (PEDOT:PSS, Clevios PH 1000, Heraeus Holding GmbH, with 5 wt% ethylene glycol, 0.1 wt% dodecylbenzenesulfonic acid, and 1 wt% of [3-glycidioxypropyl]trimethoxysilane). The thickness of the PEDOT:PSS film was \approx 250 nm. A peel-off step of the upper sacrificial layer of parylene C defined the device active area. Finally, the devices were hard baked for 60 min at 140 $^\circ\text{C}$ and immersed overnight in distilled water for the removal of any low-molecular-weight chemical compounds from the PEDOT:PSS films.

Device Characterization: All device measurements were performed with a 100 mM NaCl aqueous electrolyte at room temperature. A global Ag/AgCl electrode was placed on top of the PEDOT:PSS device with coordinates ($x = 2$ and $y = 3$) and immersed into the electrolyte. The position of the global Ag/AgCl electrode was kept constant during all measurements. The response of the devices on the grid was independent of the position of the global Ag/AgCl electrode.^[44,47] Each device on the grid was initially cycled (repetitive 0.3/−0.3 V pulse cycles at the gate for 2 s each) to obtain reproducible behavior using a 2602B SourceMeter Unit (Keithley). Device measurements were performed with a 4200A-SCS Parameter Analyzer (Keithley). A sequence of random pulses was applied at the local input $I_{x,y}$ of a device on the grid, and the output current $O_{x,y}$ was measured, with the output terminal to be connected to the ground of the Parameter Analyzer. The sampling rate of current measurement was 100 Hz. A sequence of random pulses was programmed with Python v. 3.7.0 (with amplitude $V_i = 50$ mV, width $t_p = 50$ ms, and for different pulse numbers: $N = 2\text{--}350$) using a random number generator for defining the time occurrence of the pulses. The sequence of pulses was then imported into the Parameter Analyzer as a time series of voltage pulses. Impedance spectroscopy measurements of the devices as a function of the position of the gate electrode on the device grid were performed using an AutoLab ($\mu\text{AUTOLABIII}$ potentiostat).

Analysis: $O_{x,y}$ peak analysis was performed using OriginPro 2016, with a threshold of 60% of the maximum was set for O_i peak detection, after subtracting the background noise. STFT was performed using OriginPro 2016 equipped with a Hanning-type window, with fast Fourier transform (FFT) length of 256 points and a window length of 12 points. The correlation coefficient between $O_{x,y}$ and G and correlation function between the absolute value of $O_{x,y}$ and G was calculated using OriginPro 2016.

Supporting Information

Supporting Information is available from the Wiley Online Library or from the author.

Acknowledgements

The authors wish to thank Hans-Juergen Guttmann, Christian Bauer, Frank Keller, and Michelle Beuchel from MPIP for their assistance. The authors acknowledge Kamal Asadi from MPIP for fruitful discussions on electrical measurements, Dion Khodagholy from Columbia University for fruitful discussions on neuroscience, and Aikaterini Sarafera for creating the artwork.

Conflict of Interest

The authors declare no conflicts of interest.

Keywords

electrolytes, functional connectivity, neuromorphic devices, organic electrochemical transistors, PEDOT:PSS

Received: April 4, 2019

Revised: April 8, 2019

Published online: May 8, 2019

- [1] E. R. Kandel, J. H. Schwartz, T. M. Jessell, *Principles of Neural Science*, McGraw-Hill, New York **2000**.
- [2] G. Buzsáki, B. O. Watson, *Dialogues Clin. Neurosci.* **2012**, *14*, 345.
- [3] G. Buzsáki, A. Draguhn, *Science* **2004**, *304*, 1926.
- [4] J. Fell, N. Axmacher, *Nat. Rev. Neurosci.* **2011**, *12*, 105.
- [5] G. Buzsáki, C. A. Anastassiou, C. Koch, *Nat. Rev. Neurosci.* **2012**, *13*, 407.
- [6] A. K. Engel, P. Fries, W. Singer, *Nat. Rev. Neurosci.* **2001**, *2*, 704.
- [7] F. Varela, J.-P. Lachaux, E. Rodriguez, J. Martinerie, *Nat. Rev. Neurosci.* **2001**, *2*, 229.
- [8] D. S. Gupta, L. Chen, *Curr. Opin. Behav. Sci.* **2016**, *8*, 161.
- [9] W. Singer, *Neuron* **1999**, *24*, 49.
- [10] S. N. Jacob, D. Hähnke, A. Nieder, *Neuron* **2018**, *99*, 588.
- [11] S. L. Bressler, R. Coppola, R. Nakamura, *Nature* **1993**, *366*, 153.
- [12] R. VanRullen, C. Koch, *Trends Cognit. Sci.* **2003**, *7*, 207.
- [13] A. Schnitzler, J. Gross, *Nat. Rev. Neurosci.* **2005**, *6*, 285.
- [14] C. Mead, *Proc. IEEE* **1990**, *78*, 1629.
- [15] T. Someya, Z. Bao, G. G. Malliaras, *Nature* **2016**, *540*, 379.
- [16] S. Jia, F. Ying, W. Qing, *J. Phys. D* **2018**, *51*, 314004.
- [17] Y. van de Burgt, A. Melianas, S. T. Keene, G. Malliaras, A. Salleo, *Nat. Electron.* **2018**, *1*, 386.
- [18] Y. Kim, A. Chortos, W. Xu, Y. Liu, J. Y. Oh, D. Son, J. Kang, A. M. Foudeh, C. Zhu, Y. Lee, S. Niu, J. Liu, R. Pfaltner, Z. Bao, T.-W. Lee, *Science* **2018**, *360*, 998.
- [19] S. Pecqueur, D. Vuillaume, F. Alibart, *J. Appl. Phys.* **2018**, *124*, 151902.
- [20] J. Leger, M. Berggren, S. A. Carter, *Iontronics: Ionic Carriers in Organic Electronic Materials and Devices*, CRC Press, Boca Raton **2011**.
- [21] K. Keiichi, A. Tanemasa, T. Wataru, *Jpn. J. Appl. Phys.* **1991**, *30*, L215.
- [22] V. Erokhin, T. Berzina, M. P. Fontana, *J. Appl. Phys.* **2005**, *97*, 064501.
- [23] P. Gkoupidenis, N. Schaefer, X. Strakosas, J. A. Fairfield, G. G. Malliaras, *Appl. Phys. Lett.* **2015**, *107*, 263302.
- [24] P. Gkoupidenis, N. Schaefer, B. Garlan, G. G. Malliaras, *Adv. Mater.* **2015**, *27*, 7176.
- [25] Y. van de Burgt, E. Lubberman, E. J. Fuller, S. T. Keene, G. C. Faria, S. Agarwal, M. J. Marinella, A. Talin, A. Salleo, *Nat. Mater.* **2017**, *16*, 414.
- [26] C. Wu, T. W. Kim, H. Y. Choi, D. B. Strukov, J. J. Yang, *Nat. Commun.* **2017**, *8*, 752.

- [27] G. Tarabella, P. D'Angelo, A. Cifarelli, A. Dimonte, A. Romeo, T. Berzina, V. Erokhin, S. Iannotta, *Chem. Sci.* **2015**, *6*, 2859.
- [28] W. Xu, S.-Y. Min, H. Hwang, T.-W. Lee, *Sci. Adv.* **2016**, *2*, e1501326.
- [29] A. Romeo, A. Dimonte, G. Tarabella, P. D'Angelo, V. Erokhin, S. Iannotta, *APL Mater.* **2015**, *3*, 014909.
- [30] S. Desbief, M. di Lauro, S. Casalini, D. Guerin, S. Tortorella, M. Barbalinardo, A. Kyndiah, M. Murgia, T. Cramer, F. Biscarini, D. Vuillaume, *Org. Electron.* **2016**, *38*, 21.
- [31] M. Giordani, M. Berto, M. Di Lauro, C. A. Bortolotti, M. M. Zoli, F. Biscarini, *ACS Sens.* **2017**, *2*, 1756.
- [32] S. Pecqueur, M. Mastropasqua, T. David, G. Philippe, B. J. Roncali, D. Vuillaume, F. Alibert, *Adv. Electron. Mater.* **2018**, *4*, 1800166.
- [33] Y. Lee, J. Y. Oh, W. Xu, O. Kim, T. R. Kim, J. Kang, Y. Kim, D. Son, J. B.-H. Tok, M. J. Park, Z. Bao, T.-W. Lee, *Sci. Adv.* **2018**, *4*, eaat7387.
- [34] S. Battistoni, V. Erokhin, S. Iannotta, *J. Phys. D* **2018**, *51*, 284002.
- [35] V. A. Demin, V. V. Erokhin, A. V. Emelyanov, S. Battistoni, G. Baldi, S. Iannotta, P. K. Kashkarov, M. V. Kovalchuk, *Org. Electron.* **2015**, *25*, 16.
- [36] A. V. Emelyanov, D. A. Lapkin, V. A. Demin, V. V. Erokhin, S. Battistoni, G. Baldi, A. Dimonte, A. N. Korovin, S. Iannotta, P. K. Kashkarov, M. V. Kovalchuk, *AIP Adv.* **2016**, *6*, 111301.
- [37] P. Gkoupidenis, D. A. Koutsouras, T. Lonjaret, J. A. Fairfield, G. G. Malliaras, *Sci. Rep.* **2016**, *6*, 27007.
- [38] P. Gkoupidenis, S. Rezaei-Mazinani, C. M. Proctor, E. Ismailova, G. G. Malliaras, *AIP Adv.* **2016**, *6*, 111307.
- [39] K. Duygu, Y. Shimeng, H. S. P. Wong, *Nanotechnology* **2013**, *24*, 382001.
- [40] J. Lee, W. D. Lu, *Adv. Mater.* **2018**, *30*, 1702770.
- [41] C. D. Schuman, T. E. Potok, R. M. Patton, J. D. Birdwell, M. E. Dean, G. S. Rose, J. S. Plank, Preprint at <https://arxiv.org/abs/1705.06963>, **2017**.
- [42] M. D. Pickett, G. Medeiros-Ribeiro, R. S. Williams, *Nat. Mater.* **2012**, *12*, 114.
- [43] V. Erokhin, T. Berzina, K. Gorshkov, P. Camorani, A. Pucci, L. Ricci, G. Ruggeri, R. Sigala, A. Schüz, *J. Mater. Chem.* **2012**, *22*, 22881.
- [44] P. Gkoupidenis, D. A. Koutsouras, G. G. Malliaras, *Nat. Commun.* **2017**, *8*, 15448.
- [45] D. A. Bernards, G. G. Malliaras, *Adv. Funct. Mater.* **2007**, *17*, 3538.
- [46] H. S. White, G. P. Kittleson, M. S. Wrighton, *J. Am. Chem. Soc.* **1984**, *106*, 5375.
- [47] D. A. Koutsouras, G. G. Malliaras, P. Gkoupidenis, *MRS Commun.* **2018**, *8*, 493.
- [48] N. Gupta, S. S. Singh, M. Stopfer, *Nat. Commun.* **2016**, *7*, 13808.
- [49] K. A. C. Martin, S. Schröder, *J. Neurosci.* **2016**, *36*, 2494.
- [50] S. T. Keene, A. Melianas, Y. van de Burgt, A. Salleo, *Adv. Electron. Mater.* **2018**, 1800686.
- [51] J. Y. Gerasimov, R. Gabrielsson, R. Forchheimer, E. Stavrinidou, D. T. Simon, M. Berggren, S. Fabiano, *Adv. Sci.* **2019**, *6*, 1801339.
- [52] S. E. Doris, A. Pierre, R. A. Street, *Adv. Mater.* **2018**, *30*, 1706757.
- [53] W. A. Booth, B. Edwards, K. Jo, A. Timperman, J. Schiffbauer, *Analyst* **2017**, *142*, 1554.
- [54] P. García-Sánchez, N. G. Loucaides, A. Ramos, *Phys. Rev. E* **2017**, *95*, 022802.
- [55] K. D. Jo, J. E. Schiffbauer, B. E. Edwards, R. Lloyd Carroll, A. T. Timperman, *Analyst* **2012**, *137*, 875.
- [56] G. B. Ermentrout, D. Kleinfeld, *Neuron* **2001**, *29*, 33.
- [57] J. A. Roberts, L. L. Gollo, R. G. Abeysuriya, G. Roberts, P. B. Mitchell, M. W. Woolrich, M. Breakspear, *Nat. Commun.* **2019**, *10*, 1056.